*J. Fluid Mech.* (1990), *vol.* 213, *pp.* 589–610
*Printed in Great Britain*



# Oscillatory motion in a side-heated cavity

By S. G. SCHLADOW†
Environmental Fluid Mechanics Laboratory, Department of Civil Engineering, Stanford University, Stanford, CA 94305-4020, USA

(Received 28 March 1989 and in revised form 18 August 1989)

Direct numerical simulations of the transient flow in a side-heated cavity have been conducted for a Rayleigh Number of $2 \times 10^9$, an aspect ratio of 1 and a Prandtl Number of 7.1. The results show the presence of both long-period and short-period oscillations. The long-period oscillation is a cavity-scale mode produced by the tilting of the isotherms. The short-period oscillations are shown to be the result of two distinct boundary-layer instabilities. Whereas the latter oscillations can produce large deviations in the observed temperature records, they are relatively shortlived and have only a minor influence on the evolution of the flow towards steady state. The suggestion of the existence of an internal hydraulic jump in such flows has been investigated and found to be incorrect.

## 1. Introduction

Oscillatory motion in a cavity subjected to a temperature difference applied between two vertical sidewalls has been the subject of a number of studies. Oscillation superimposed on a steady convective flow has been addressed both experimentally (Hurle, Jakeman & Johnson 1974) and theoretically (Gill 1974) with the latter giving a feasible explanation of why oscillations should occur. When the underlying convective flow is unsteady, as would be the case in many natural flow situations, agreement as to the origins of the oscillation appears to have been more elusive. The flow regime that forms the focus of the present study is a case in point. Though certainly not the only regime in which oscillations would be present as part of the transient flow, it is interesting in that the oscillation timescale suggested by theoretical considerations is an order of magnitude larger than some of the oscillations observed to date. A brief chronology provides a background to the present study.

Patterson & Imberger (1980) suggested that a cavity-scale internal seiche may be produced by the tilting of isotherms as the hot and cold intrusions ejected from the vertical wall boundary layers cross the cavity and then spread to match the entrainment towards the opposite vertical wall. The approach to steady state would then include a damped oscillation. (This is the large-timescale oscillation.) A set of experiments by Ivey (1984), designed to test this hypothesis, found no convicing evidence of regular cavity-scale oscillations. Temperature traces, however, clearly showed a short-period, large-amplitude oscillation for part of the time. The source of these oscillations was suggested to be 'the inertia of the flow entering the interior of the cavity from the sidwall boundary layers, which may lead to a form of internal hydraulic jump...'. Numerical simulations based on Ivey's experiments were

† Present address: Centre for Limnological Modelling, Department of Civil and Environmental Engineering, University of Western Australia, Nedlands, Western Australia, 6009.

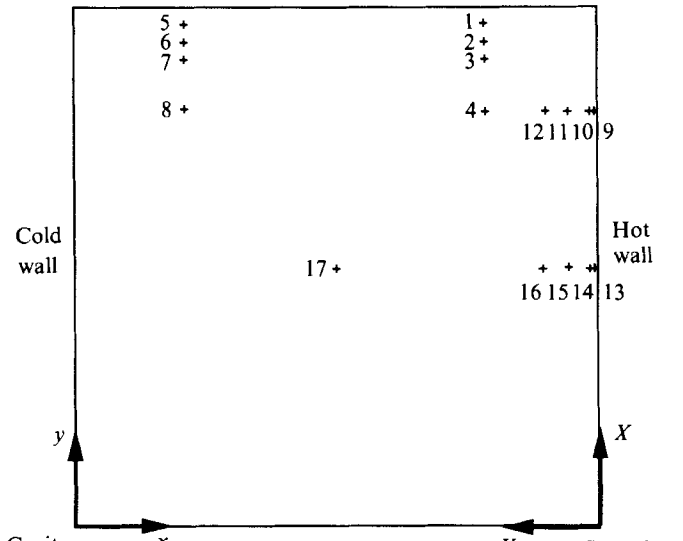


| Point | $x/l$ | $y/h$ | 6 | 0.21 | 0.937 | 12 | 0.90 | 0.80 |
|---|---|---|---|---|---|---|---|---|
| 1 | 0.79 | 0.967 | 7 | 0.21 | 0.90 | 13 | 0.997 | 0.50 |
| 2 | 0.79 | 0.937 | 8 | 0.21 | 0.80 | 14 | 0.990 | 0.50 |
| 3 | 0.79 | 0.90 | 9 | 0.997 | 0.80 | 15 | 0.95 | 0.50 |
| 4 | 0.79 | 0.80 | 10 | 0.990 | 0.80 | 16 | 0.90 | 0.50 |
| 5 | 0.21 | 0.967 | 11 | 0.95 | 0.80 | 17 | 0.50 | 0.50 |

FIGURE 1. General arrangement of simulated cavity. Coordinate axes $(x, y)$ refer to the cavity. Coordinate axes $(X, Y)$ refer to the hot-wall boundary-layer only. Points indicate locations at which temperature, velocity and vorticity are recorded at every timestep.

conducted by Schladow, Patterson & Street (1989, henceforth referred to as SPS). These clearly showed the presence of the long-period oscillation; however, there was virtually no evidence of short-period oscillations. The mechanism producing the oscillations was seen to be a combination of the isotherm tilting postulated by Patterson & Imberger, as well as tilting due to a simple 'piling up' of the intrusion fluid. Paolucci & Chenoweth (1989) also conducted numerical simulations based on Ivey's experiments, and by contrast observed the short-period oscillations and not the long-period ones. They concurred with the hypothesis of the internal hydraulic jump producing the observed oscillations. Reference was also made to a further episode of oscillation at a relatively late stage in the transient; however no data were presented to indicate its nature.

This contribution seeks to reconcile the differences in the observations (both experimental and numerical) by proposing that both the long-period and the short-period oscillations exist as part of this regime. The former are of the type suggested by Patterson & Imberger (1980) and SPS. The latter, however, will be shown to be the result of two distinct instabilities in the vertical boundary layers rather than being associated with any kind of internal hydraulic jump.

## 2. Problem description

The system we consider is a closed, two-dimensional rectangular cavity as shown in figure 1. The upper and lower boundaries are insulated and at time $t = 0$ the right-

and left-hand walls are instantaneously heated and cooled respectively and thereafter maintained at constant temperature. The equations of mass, momentum (horizontal and vertical) and energy conservation which describe the ensuing motion and which are used as the basis of the discretized equations we later solve are

$$\partial(\rho u)/\partial x + \partial(\rho v)/\partial y = 0, \tag{1}$$

$$\partial u/\partial t + u\,\partial u/\partial x + v\,\partial u/\partial y = -(1/\rho)\,\partial p/\partial x + \nu\nabla^2 u, \tag{2}$$

$$\partial v/\partial t + u\,\partial v/\partial x + v\,\partial v/\partial y = -(1/\rho)\,\partial p/\partial y + \nu\nabla^2 v + g\alpha(T - T_0), \tag{3}$$

$$\partial T/\partial t + u\,\partial T/\partial x + v\,\partial T/\partial y = \kappa\nabla^2 T, \tag{4}$$

where $u$ and $v$ are the velocity components in the $x$- and $y$-directions respectively, $T$ is the temperature, $p$ is the pressure deviation from that at hydrostatic equilibrium and $\nu$, $\rho$, $\alpha$ and $\kappa$ are respectively the kinematic viscosity, density, coefficient of thermal expansion and thermal diffusivity of the fluid. The acceleration due to gravity is positive in the $-y$-direction.

The Boussinesq assumption has not been invoked insofar as the effect of temperature on density and all other fluid properties has been explicitly retained in all terms of the above equation set. The temporal term in the mass conservation equation has, however, been neglected, as it was found to impair rapid convergence of the numerical scheme while having a negligible influence on the solution accuracy.

The initial conditions may be written as

$$u(x, y, 0) = v(x, y, 0) = 0, \quad T(x, y, 0) = T_0 \tag{5}$$

and the boundary conditions applied at $t \geqslant 0$ may be written as

$$\left.\begin{aligned} u(0, y, t) = u(l, y, t) = u(x, 0, t) = u(x, h, t) = 0, \\ v(x, 0, t) = v(x, h, t) = v(0, y, t) = u(l, y, t) = 0, \\ T(0, y, t) = T_0 - \Delta T, \quad T(l, y, t) = T_0 + \Delta T, \\ \partial T/\partial y(x, 0, t) = \partial T/\partial y(x, h, t) = 0, \end{aligned}\right\} \tag{6}$$

where $h$ and $l$ are the cavity height and length respectively.

The flow is a function of three dimensionless parameters: the Rayleigh number $Ra$, the Prandtl number $\sigma$, and the aspect ratio $A$. These are defined as

$$Ra = 2g\alpha\Delta T h^3/\nu\kappa, \tag{7}$$

$$\sigma = \nu/\kappa, \tag{8}$$

and

$$A = h/l. \tag{9}$$

For the case of a shallow cavity ($A \leqslant 1$) with a Prandtl number greater than unity ($\sigma > 1$) and satisfying the condition $A^{-6} < \sigma$, Patterson (1984) showed there were six possible flow regimes, each demarcated by a critical value of $Ra$. We consider Regime V, which lies in the Rayleigh-number range $\sigma^{10} < Ra < \sigma^{16}A^{-12}$. In particular we adopt the case of a square cavity, with $h = l = 0.24$ m, and initial temperature $T_0 = 20$ °C and a temperature difference $\Delta T = 5$ °C. Water is the assumed working fluid with a Prandtl number at 20 °C of 7.1. The Rayleigh number is $2 \times 10^9$. These values nominally coincide with those used by Ivey (1984). The flow regime and parameter values considered could conceivably be realized in the growth of crystals from aqueous solutions using horizontal growth techniques. Similar processes could also be expected with different values of aspect ratio and Prandtl number (Patterson 1984) thus making the processes of considerable practical interest.

## 3. Previous work

Some of the previous work relating to transient flows in side-heated cavities has already been alluded to in the Introduction. This will now be enlarged upon.

The scaling analysis of Patterson & Imberger (1980) was the first attempt to quantitatively describe and classify the transient flows in shallow, side-heated cavities. Their numerical solution of the flow equations confirmed the scaling results in the low-*Ra* regimes. The numerical results of Gresho *et al.* (1980) also provided independent corroboration of many of the results, including the existence of a long-period internal wave mode. Although the higher-*Ra* regimes were not solved numerically, the mechanism of internal wave production was the same for the lower- and higher-*Ra* regimes, and consequently it was believed that similar oscillations would exist.

The scaling analysis for the higher-*Ra* regimes (for example Regime V) suggests the following transient flow evolution for the present parameters. Immediately after the temperature difference is imposed, a double-layer structure starts to form on the vertical walls. The timescale for its growth is $O(10\text{ s})$, with the lengthscales for the outer viscous layer and the inner thermal layer being approximately 3 mm and 1 mm respectively. As the flow along a vertical wall approaches a corner, it is forced to discharge into the core of the cavity. Heated (cooled) fluid then intrudes as a relatively fast moving layer across the top (bottom) of the cavity. The mass flux associated with each intrusion is supported by entrainment into the vertical boundary layer along its entire length. As an intrusion approaches the opposite side of the cavity it spreads to match the entrainment demand and in so doing its isotherms are tilted (with a positive slope) beyond the horizontal. The horizontal pressure gradient produced induces a cavity-scale internal wave (seiche) in the stratified portion of the cavity, resulting in the oscillation of the isotherm slope about the vertical centreline of the cavity. Eventually the seiche decays. As the flow continues there is a gradual filling of the core with a stable vertical temperature gradient, until a steady state is achieved.

This regime was first examined experimentally by Ivey (1984). As noted previously, the experiments confirmed much of this description, but differed in two major regards. First, they showed no evidence of the long-period internal wave. The data on which this conclusion was drawn, however, were limited to temperature traces from three thermistor probes located close to the top of the cavity. These are shown as points 1, 2 and 5 in figure 1. The presence of a temperature inversion and a complex recirculating region near the top of the hot wall, as shown by SPS, make the observation of such a wave by thermometry at these points virtually impossible. In comparison, by calculating the heat flux across the vertical centreline of the cavity (where the horizontal velocity would have a very pronounced oscillatory signal in the presence of a seiche) SPS showed clearly and unambiguously the existence of a decaying seiche with a period of 60–70 s, close to the predicted period.

Second, the experimental thermistor traces did display a short-period oscillation with a period of approximately 5–6 s and peak-to-peak amplitude of $\sim 0.4\Delta T$. This amplitude is several times larger than the seiche amplitude produced by SPS. The existence of these oscillations cannot be disputed; however, the mechanism for their production could only be guessed at by Ivey. His suggestion of an 'internal hydraulic jump' (the previously referred to 'complex recirculating zone') as the probable source of these fluctuations, was based on an order of magnitude calculation. Similar flow features have been open to different interpretation by other investigators (see

for example Worster & Leitch 1985). The SPS simulations showed almost no trace of these short-period oscillations although a flow structure of similar appearance was present near the top of the hot wall. Calculations based on the numerical results suggested that the internal Froude number, $F$, just upstream of the 'jump' location was in the range 0.7–1.5 indicating that, if indeed a hydraulic jump existed ($F > 1$), it would be undular ($1.0 < F < 1.7$) and take the form of smooth standing waves with small energy losses.

The recent simulation by Paolucci & Chenoweth (1989) agrees with the experiment in that short-period oscillations are observed while long-period oscillations are not. The latter point is readily explained in that the evidence for a long-period oscillation was sought only at the measurement points used in the experiments, and the numerical results therefore have the same shortcoming as the experiments. Paolucci & Chenoweth's failure to observe a seiche under other flow conditions may be attributable to the initial conditions employed in the simulations. Rather than using an isothermal state, these conditions consisted of the steady-state temperature fields of lower-$Ra$ flows. The detrainment that occurs from a boundary layer when the ambient is stratified (Gill 1966) serves to weaken the intrusion flows at the top and bottom of the cavity, and the smaller entrainment length reduces the propensity for the isotherms to tilt. This latter effect is reinforced by the presence of the vertical density gradient, which generally suppresses the 'piling up' of the intrusions (Schladow & Street 1988).

The observation of the short-period oscillation by Paolucci & Chenoweth clearly is at odds with SPS. As will be shown in the subsequent sections, the failure of the SPS simulation to resolve these small-scale features is due to numerical diffusion. However, the diffusion's effect on the large-scale features which were the focus of that study was very slight. The observation of these oscillations, however, does little to advance our understanding of their cause. Although Paolucci & Chenoweth agree with Ivey's hydraulic jump mechanism, the value of the Froude number they report is 0.63, well below the limit for a hydraulic jump. Their results did, however, suggest that the oscillations were stronger near the emergent corners than away from them. In view of the low Froude number, the most likely place to look for the source of these oscillations is, therefore, the region of flow generation, namely, the vertical boundary layers.

At high Rayleigh numbers the boundary layers are thin compared to the cavity dimension and so the vertical boundaries can be thought of as existing in an extensive medium ($l \to \infty$). (This assumption was central to the earlier scaling analysis by Patterson & Imberger 1980.) Employing the usual boundary-layer approximations, together with the Boussinesq approximation, one can readily show that the equation set (1)–(4) reduces to the following set in the vicinity of the hot wall:

$$\partial U/\partial X + \partial V/\partial Y = 0, \tag{10}$$

$$\partial U/\partial t + U\partial U/\partial X + V\partial U/\partial Y = \nu\partial^2 U/\partial Y^2 + g\alpha(T - T_0), \tag{11}$$

$$\partial T/\partial t + U\partial T/\partial X + V\partial T/\partial Y = \kappa\partial^2 T/\partial Y^2. \tag{12}$$

As shown in figure 1, the $X$- and $Y$-axes in these equations are not the same as those used to describe the whole cavity flow. These transformed axes are adopted primarily to conform with the conventions of the boundary-layer literature. Similarly, reference will also be made to the Grashof number, $Gr = Ra/\sigma$. $U$ and $V$ are the velocity

components in the $X$- and $Y$-directions, respectively. The appropriate initial and boundary conditions are

$$U(X,Y,0) = V(X,Y,0) = 0, \quad T(X,Y,0) = T_0 \tag{13}$$

and

$$\left.\begin{aligned} &U(0,Y,t) = V(0,Y,t) = 0, \quad U(X,0,t) = V(X,0,t) = 0,\\ &T(0,Y,t) = T_0, \quad T(X,0,t) = T_0 + \Delta T,\\ &T(X,\infty,t) = T_0, \quad U(X,\infty,t) = 0. \end{aligned}\right\} \tag{14}$$

These are the same equations that apply to the well-studied problem of a semi-infinite heated plate; hence many of the results that apply to it may be expected to have application to our problem. However, as the flow proceeds, the boundary conditions as $Y \to \infty$ will diverge from the above as the effects of the internal nature of the flow become felt.

No analytical solution exists for the temporal behaviour of a laminar flow past a semi-infinite plate following a step change in temperature. Following Brown & Riley (1973), it can be considered as occurring in a number of stages. Initially, the heat transfer from the wall to the fluid is purely by conduction and, hence, a one-dimensional solution describes the flow. This abruptly ends with the passage of the 'leading edge' influences, followed by an asymptotic approach to the classical steady-state flow. At some distance downstream (corresponding to a sufficiently high Grashof number) the laminar boundary layer becomes unstable to disturbances in the flow. These disturbances amplify and eventually through nonlinear interactions may result first in a transitional flow and eventually in a fully developed turbulent flow. Depending on the flow conditions, the boundary layer may relaminarize at its fully developed state or may remain turbulent (Mollendorf & Gebhart 1970).

The initial phase is a consequence of the fact that sufficiently far from the leading edge, the fluid acts as if the plate was doubly infinite, with a velocity distribution independent of $X$ (Siegel 1958). Hence the convective heat transfer is zero and the velocity is a function of time and distance from the heated boudary. The two-dimensional influence which causes the boundary layer growth to vary with $X$ propagates away from the leading edge. The beginning of convective heat transfer at a particular $X$ commences only after this leading-edge influence has reached that point, after being advected along the boundary layer by the fastest moving fluid. Goldstein & Briggs (1964) present solutions for predicting when the leading-edge effect will penetrate a given distance $X_p$, based on the velocity and temperature fields along a doubly infinite plate. For $\sigma > 1$, their solutions for the one-dimensional temperature and velocity fields and for the penetration distance are

$$T = (T_0 + \Delta T)\operatorname{erfc}\zeta, \tag{15}$$

$$U = \frac{4g\alpha(T_0+\Delta T)\,t}{\sigma-1}\left[\mathrm{i}^2\operatorname{erfc}\zeta - \mathrm{i}^2\operatorname{erfc}\frac{\zeta}{\sigma^{0.5}}\right], \tag{16}$$

$$X_p = \frac{16g\alpha(T_0+\Delta T)\,t^2}{\sigma-1}\left[\mathrm{i}^4\operatorname{erfc}\zeta - \mathrm{i}^4\operatorname{erfc}\frac{\zeta}{\sigma^{0.5}}\right], \tag{17}$$

where $\zeta = Y/(4\kappa t)^{0.5}$ is the dimensionless $Y$-coordinate and $\mathrm{i}^n\operatorname{erfc}\zeta$ is the $n$th integral of $\operatorname{erfc}\zeta$. The penetration distance, $X_p$, was maximized over $Y$, at a given $t$, such that $X_p = \max\left[\int_0^t U(Y,t)\,\mathrm{d}t\right]$. By contrast, Brown & Riley (1973) give $X_p = \int_0^t \{\max\left[U(Y,t)\right]\mathrm{d}t\}$ which yields a propagation rate that is only slightly faster than that of Goldstein & Briggs. A number of numerical results have shown

departures from the one-dimensional solution earlier than either of these formulations suggest (Ingham 1978, for example). In addition, Ingham (1978, 1985) demonstrates the discontinuous nature of the transition from the one-dimensional to the steady solution. Direct measurements by Joshi & Gebhart (1987) confirm that the 'leading edge' effect arrives abruptly and somewhat earlier than indicated by (17). For wall lengths commensurate with our cavity dimensions, its manifestation took the form of a sinusoidal disturbance to both the temperature and velocity fields, which when measured at a point had a duration of 2–3 periods.

The laminar, steady-state solutions for temperature and velocity adjacent to a semi-infinite heated plate was obtained numerically by Ostrach (1952), using similarity techniques. In terms of the similarity variable $\eta = (\frac{1}{4}Gr_x)^{\frac{1}{4}} Y/X$, where the Grashof number $Gr_x = g\alpha\Delta T X^3/\nu^2$, it was shown that

$$\frac{UX/\nu}{2(Gr_x)^{\frac{1}{2}}} = F'(\eta), \tag{18}$$

$$\frac{T-T_0}{\Delta T} = H(\eta). \tag{19}$$

Values of $F'$ and $H$ were tabulated for different values of $\sigma$. The good agreement between these solutions and experimental data is summarized by Ede (1967).

The development of disturbances in boundary-layer flows has been the subject of a large body of work. Much of this is summarized in reviews by Gebhart (1973) and Gebhart & Mahajan (1982), and will only briefly be described here. Using linear stability analyses, values of $G$, the modified Grashof number, as a function of $\Omega$, a generalized frequency, can be found for the case of neutral stability. Contours of constant amplification rate in the unstable region can also be readily determined. For the case of a step change in boundary temperature,

$$\Omega = \frac{(2\pi f)\,\delta G^{\frac{1}{3}}}{U_c} \tag{20}$$

and

$$G = 4(\tfrac{1}{4}Gr_x)^{\frac{1}{4}}. \tag{21}$$

The characteristic base flow velocity, $U_c$, and characteristic boundary-layer thickness, $\delta$, are given by

$$\frac{U_c X}{\nu} = \tfrac{1}{4}G^2 \tag{22}$$

and

$$\delta = \frac{4X}{G} \tag{23}$$

respectively, and $f$ is the disturbance frequency.

The analyses show that the flows are highly selective in their amplification characteristics. A wide-band disturbance is band-pass filtered for a very narrow frequency band as it is convected downstream. This frequency band coincides with the most rapidly amplified frequencies. A single-frequency disturbance is either poorly amplified if it is away from this band (but still within the unstable region) or strongly amplified if close to it. Experimental results strongly support this notion of selectivity in amplification and consistently show nearly sinusoidal disturbances being advected downstream by the boundary-layer flow. This applies to both initially steady flows that are artificially perturbed (Jaluria & Gebhart 1973) and to the early stages of transient flow referred to earlier. Although most experiments have

been conducted for the experimentally more convenient arrangement of a constant-heat-flux surface, the exact nature of the base flow is not an important determinant of the disturbance characteristics and this description may be considered as basically correct for the isothermal case too (Gebhart 1969).

The continued development of the flow through transition and finally to turbulence will not be reviewed. The usual criteria for the observation of these states – higher-frequency components superimposed on the laminar filtered frequency, and departures from the laminar temperature and velocity profiles (Gebhart & Mahajan 1982) – were not observed in the present study, as will be shown below. Furthermore, the particle track photographs from Ivey (1984) all show smooth pathlines, strongly suggestive of laminar flow throughout the transient. (These may be contrasted with those of Joshi & Gebhart (1987), where far more erratic pathlines are present during transition and turbulence.) The thermistor traces produced by Ivey, though containing a 5–6 s oscillation, do not suggest a turbulent flow.

## 4. Numerical procedures

All numerical results to be presented were obtained using the SEAFLOS1 code. A complete description of it is given by Perng & Street (1989). The code solves the finite-differenced forms of equations (1)–(4) on a spatially non-uniform grid in two dimensions. Though having its origins in the SIMPLE algorithm (Patankar 1980), SEAFLOS1 differs in some fundamental respects. These differences relate primarily to the use of quadratic upstream interpolation (the QUICK algorithm; see Leonard 1979) for the convective terms and a conjugate gradient scheme for the solution of an exact pressure equation. Whereas the version of SEAFLOS1 used by SPS advanced in time by using a first-order-accurate implicit Euler scheme, time advancement is now by an explicit, second-order predictor-corrector scheme.

Consideration was given to solving the equations in three spatial dimensions, as had been done by SPS. However, their results suggested that three-dimensional effects at the cavity-scale level only became apparent for times much larger than those that are the focus of the present paper. As the results to be presented agree sufficiently well with observations (both for cavities and vertical plates) and bearing in mind that the computational cost of a three-dimensional simulation would be high, the decision to proceed with only two-dimensional simulations appears to be *a posteriori* justified.

In seeking to perform time-accurate simulations of a transient flow, the minimization of artificial viscosity is a major consideration. An estimate of it can readily be obtained by first representing a model continuum equation in finite-difference form and then expanding in a Taylor series the terms of this finite-difference equation (Hirt 1968). This generates a second continuum equation which, when compared to the model equation, reveals the artificial viscosity induced by the particular differencing scheme chosen. For this purpose it is sufficient to use the unsteady advection–diffusion equation, $\partial\phi/\partial t = -u\,\partial\phi/\partial x + D\,\partial^2\phi/\partial x^2$, as a model equation. Here, $\phi$ is the variable to be solved for, $D$ is the 'natural viscosity' coefficient (kinematic viscosity if $\phi$ is a velocity component) and the other terms are as defined previously. Table 1 lists the generated continuum equations for a number of possible differencing schemes. The spatial difference schemes considered are central differencing (CD), conventional upwind differencing (UD) and quadratic upwind differencing (QD), while the temporal schemes are explicit Euler (EE), implicit Euler (IE) and predictor-corrector (PC). The terms $\Delta t$ and $\Delta x$ are the

| Algorithm | Continuum equation |
|---|---|
| CD+EE | $\frac{\partial\phi}{\partial t} = -u\frac{\partial\phi}{\partial x} + (\nu - \frac{1}{2}u^2\Delta t)\frac{\partial^2\phi}{\partial x^2}$ |
| CD+IE | $\frac{\partial\phi}{\partial t} = -u\frac{\partial\phi}{\partial x} + (\nu + \frac{1}{2}u^2\Delta t)\frac{\partial^2\phi}{\partial x^2}$ |
| UD+IE | $\frac{\partial\phi}{\partial t} = -u\frac{\partial\phi}{\partial x} + (\nu + \frac{1}{2}u^2\Delta t + \frac{1}{2}u\Delta x)\frac{\partial^2\phi}{\partial x^2}$ |
| QD+EE | $\frac{\partial\phi}{\partial t} = -u\frac{\partial\phi}{\partial x} + (\nu - \frac{1}{2}u^2\Delta t)\frac{\partial^2\phi}{\partial x^2}$ |
| QD+IE | $\frac{\partial\phi}{\partial t} = -u\frac{\partial\phi}{\partial x} + (\nu + \frac{1}{2}u^2\Delta t)\frac{\partial^2\phi}{\partial x^2}$ |
| QD+PC | $\frac{\partial\phi}{\partial t} = -u\frac{\partial\phi}{\partial x} + \left(\nu + \frac{2\nu^2\Delta t}{\Delta x^2}\right)\frac{\partial^2\phi}{\partial x^2}$ |

TABLE 1. Generated continuum equations for particular algorithms. CD = central differencing; UD = upwind differencing; QD = quadratic upstream differencing; EE = explicit (forward) Euler; IE = implicit (backward) Euler; PC = predictor-corrector.

| | | | Corner | | | Wall | | |
|---|---|---|---|---|---|---|---|---|
| Mesh | Algorithm | $\Delta t$ | $\Delta x$ | Vel | $D'/D$ | $\Delta x$ | Vel | $D'/D$ |
| 50 × 50 | QD+IE | 1.0 | 0.001 | 0.001 | 0.5 | 0.009 | 0.01 | 50 |
| 50 × 50 | QD+PC | 0.02 | 0.001 | 0.001 | 0.04 | 0.009 | 0.01 | 0.0005 |
| 90 × 90 | QD+IE | 0.25 | 0.0004 | 0.001 | 0.1 | 0.005 | 0.01 | 12 |
| 90 × 90 | QD+PC | 0.005 | 0.0004 | 0.001 | 0.06 | 0.005 | 0.01 | 0.0004 |
| 130 × 130 | QD+PC | 0.005 | 0.0004 | 0.001 | 0.06 | 0.002 | 0.01 | 0.002 |

TABLE 2. Ratio of numerical viscosity to 'natural' viscosity, $D'/D$, adjacent to the vertical wall and in a corner region. The value of $D$ corresponds to the kinematic viscosity of water at 20 °C. $\Delta t$ is the timestep (s); $\Delta x$ is the mesh size (m); Vel is a typical velocity ($ms^{-1}$).

temporal and spatial step sizes used in the finite-difference formulations. Of the spatial differencing methods, neither CD nor QD generates artificial viscosity. Conventional UD does make a contribution, as evidenced by the additional coefficients of the second derivative term. All of the temporal differencing methods have an artificial viscosity component. However, the contribution associated with the PC scheme is far smaller for the conditions pertaining to our problem. This can be seen in table 2, where the ratio of the artificial viscosity term to the 'natural' viscosity term, $D'/D$, for the PC and the IE schemes is compared for a number of meshes and time steps. Estimates are provided for the wall and the corner regions, as these regions are the most critical in terms of describing the flow, and significantly different velocities and mesh sizes pertain to each of these regions. The $\Delta x$ used for each case is the mesh size half-way up the vertical wall (in the case of the wall region) and the mesh size approximately $0.01h$ from the corner (for the corner region). The maximum and minimum velocities are order of magnitude estimates for the wall and corner regions.

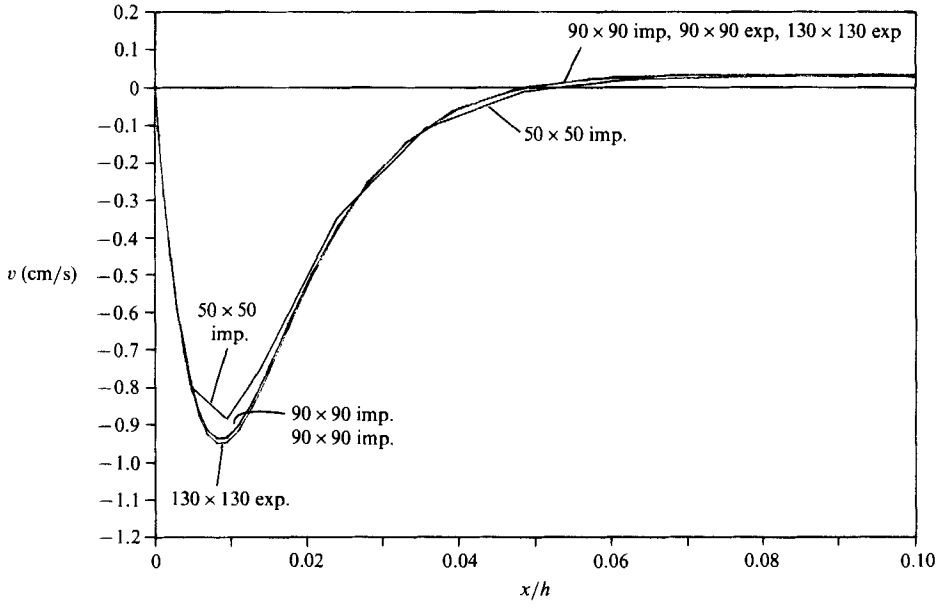


FIGURE 2. Profiles of vertical velocity normal to the midpoint of the cold boundary at $t = 20$ s.

It is clear from table 2 that the predictor-corrector scheme produces the smaller values of artificial viscosity for both regions. The corner values are somewhat higher than those along the wall; however, they are still negligible. The implicit Euler scheme, by contrast, produces its larger values (for a particular $\Delta t$) in the regions of highest velocity, i.e. at locations adjacent to the vertical wall. The estimated values are actually larger than the 'natural' viscosity.

The implications of this result are potentially significant, considering that it is just this scheme that was used by SPS. If the velocity were predominantly along the boundary (as would be the case in a boundary layer) and generally unperturbed, the effect of the higher viscosity would still be negligible, as the $\partial^2\phi/\partial x^2$ term itself would be very small, i.e. flow is dominated by the advection terms. Therefore, even with the relatively high level of artificial diffusivity in this region, the effect would be minor. This was the argument advanced by SPS. The soundness of the argument is made evident in figure 2, where velocity profiles adjacent to the midheight of the cold boundary are shown at $t = 20$ s for four of the cases considered in table 2. The profiles of both explicit cases and the $90 \times 90$ implicit case are coincident, indicating the negligible effect of longitudinal diffusion. If, however, the boundary layer were subject to small perturbations, the locally high value of the $\partial^2\phi/\partial x^2$ term in the region of the disturbance would lend significance to the viscous term. One would, as a consequence, expect that these disturbances would suffer damping. Thus, any effect of such perturbations would be lost to a simulation using the implicit Euler scheme.

In order to be sure that perturbations in the vertical boundaries could be resolved, a comparison was conducted between a $130 \times 130$ mesh and a $90 \times 90$ mesh, both using the explicit predictor-corrector time advancement. The $130 \times 130$ mesh had the same number of points as the $90 \times 90$ code in the vicinity of the boundaries (7 points within the thermal boundary-layer thickness and 11 points within the viscous boundary layer thickness), but up to double the points away from the boundaries. In

this way the mesh spacing along the vertical boundaries (the $y$-direction) was increased, especially near the midheight. As the perturbations were believed to be of a similar size to the boundary-layer thicknesses, the resolution normal to the vertical boundaries (the $x$-direction) was considered ample. Virtually no difference in the flows was observed for the time sequence 0–40 s when both codes were run. This includes a period during which boundary-layer perturbations do exist. Figure 2 shows the close agreement between the velocity profiles adjacent to the cold wall at $t = 20$ s for each of the meshes. As a consequence, the extension of the numerical results to 400 s was only done for the $90 \times 90$ explicit code, and all the results that follow were taken from the resulting data set. All runs were conducted at the San Diego Supercomputer Center, using a Cray X/MP. Typical CPU time for a timestep with the $90 \times 90$ mesh was 1.6 s.

## 5. Results

### 5.1. *Boundary layers*

The results that follow are from the boundary layer adjacent to the heated wall. However, similar results were also observed at corresponding times and positions adjacent to the cooled wall. Traces of temperature and vertical velocity against time are shown in figures 3 and 4 at five points with fixed values of the similarity variable, $\eta$ (defined just prior to (18)). In figure 3, $\eta = 0.3$ and in figure 4, $\eta = 0.8$. It is evident from successive curves on both figures that there are indeed oscillations present in the boundaries and that they are progressively amplified. Their origins, however, are not so evident.

The first packet of oscillations on each curve correspond to the 'leading-edge' effect. The rapid buildup of velocity and temperature just prior to this event is consistent with (15) and (16). For example, the top curve in all the figures is the one-dimensional solution for the points at $X/h = 0.8$. Further, the extent to which the individual curves overlay each other prior to the arrival of the disturbance confirms the underlying assumption that the response is one-dimensional at that time. The time at which the penetration distance, $X_p$, was calculated to have reached each point is also plotted as a solid circle on each curve. In all cases it can be seen that the calculated time from (17) was longer than the time at which the numerical results first separated from the one-dimensional response, a result similar to the experimental results of Joshi & Gebhart (1987) and the numerical results of Ingham (1978).

The oscillations themselves also agree with much of the previous literature. Their effect on the temperature and velocity fields is identical to that found by Joshi & Gebhart (1987) and they conform to the postulated discontinuity between the one-dimensional and steady solutions (Brown & Riley 1973; Ingham 1985). There is a distinct selective amplification, with the preferred period being typically 6 s. In their figure 5, Gebhart & Mahajan (1982) have assembled data from a number of heated-plate experiments. For $\sigma = 7.1$, the figure shows a generalized frequency $\Omega$ of 0.25 being the most rapidly amplified. Using (20)–(23) with a temperature difference of 5 °C applied at the wall, this $\Omega$-value is readily shown to correspond to a disturbance frequency, $f$, of approximately 0.18 Hz, or a period of 5.6 s. For a point midway up the wall, the numerical results show the periods to be generally in the range 5.1–6.0 s, although at the front of the packet the period tends to be stretched (to as long as 8.7 s). The temperature disturbance propagates first, with horizontal velocity component, vertical velocity component and vorticity having approximate phase lags of 2.0, 0.8 and 0.5 s respectively.

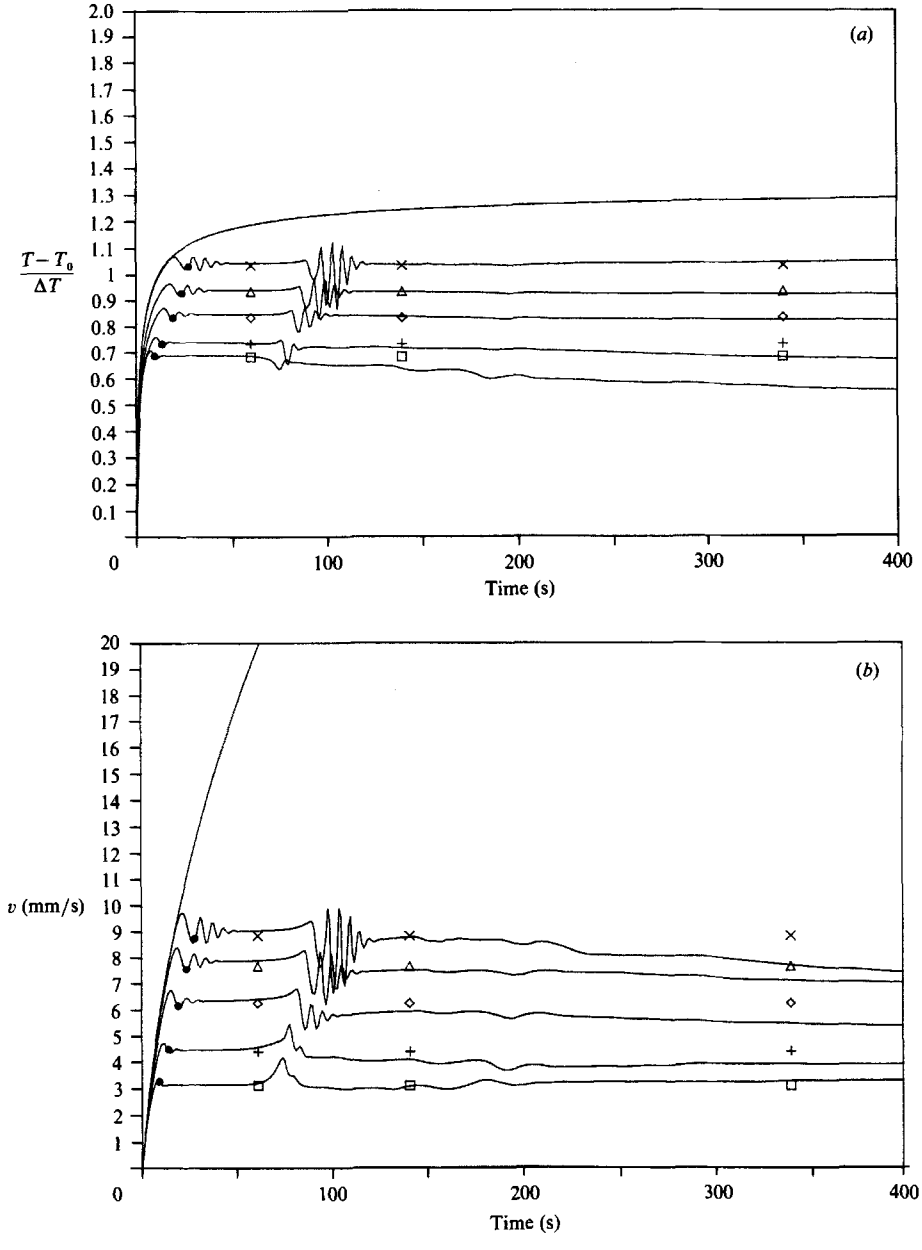


FIGURE 3. Time traces of dimensionless temperature and vertical velocity component at five points with $\eta = 0.3$. From the bottom, the points are at $(x/h, y/h)$-coordinate values (0.9979, 0.1), (0.9975, 0.2), (0.9971, 0.4), (0.9967, 0.6) and (0.9965, 0.8). The top curve is the one-dimensional solution for (0.9965, 0.8). The solid circle (●) represents the calculated arrival time of the leading-edge effect. The other symbols at $t = 60$, 140 and 340 s are the steady-state values at each of the above coordinates. (*a*) $(T-T_0)/\Delta T$ against time. The ordinate scale refers to the lowest trace and its steady-state value. Traces for successive points are staggered by 0.05, 0.15, 0.25 and 0.35 respectively. (*b*) Vertical velocity component, $v$, against time.

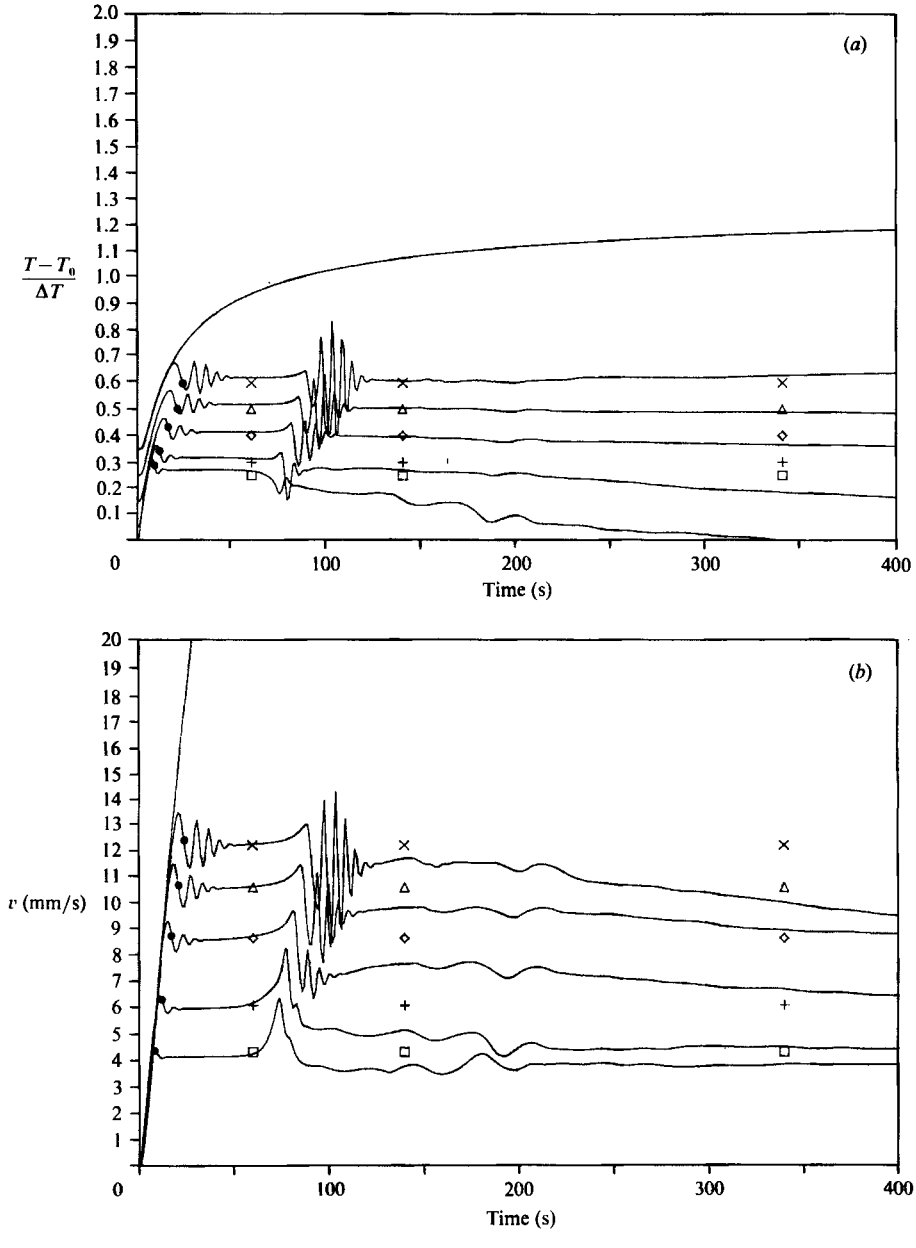


FIGURE 4. Time traces of dimensionless temperature and vertical velocity component at five points with $\eta = 0.8$. From the bottom, the points are at $(x/h, y/h)$-coordinate values (0.9945, 0.1), (0.9934, 0.2), (0.9921, 0.4), (0.9913, 0.6) and (0.9907, 0.8). The top curve is the one-dimensional solution for (0.9907, 0.8). The solid circle (●) represents the calculated arrival time of the leading-edge effect. The other symbols at $t = 60$, 140 and 340 s are the steady-state values at each of the above coordinates. (*a*) $(T-T_0)/\Delta T$ against time. The ordinate scale refers to the lowest trace and its steady-state value. Traces for successive points are staggered by 0.05, 0.15, 0.25 and 0.35 respectively. (*b*) Vertical velocity component, $v$, against time.

As well as the increase in disturbance amplitude along a constant-$\eta$ line, the disturbance size also varies with $\eta$. For example, the amplitude of the temperature disturbances due to the 'leading-edge' effect at $X/h = 0.8$ in figures 3(*a*) and 4(*a*) corresponds to temperature fluctuations of 0.25 and 0.5 °C respectively. A similar increase in vertical velocity component can also be seen in figures 3(*b*) and 4(*b*). The symbols shown at $t = 60$, 140 and 340 s in figures 3 and 4 are the steady-state values of velocity and temperature calculated from (18) and (19), using interpolation of Ostrach's (1955) tabulated data for $F'$ and $H$. For $\eta = 0.3$, the interpolation equations used were

$$F' = 0.0861(\sigma/10)^{-0.2545}, \quad H = 0.6534(\sigma/10)^{-0.1146},$$

and for $\eta = 0.8$ they were

$$F' = 0.1137(\sigma/10)^{-0.3583}, \quad H = 0.2406(\sigma/10)^{-0.4930}.$$

While the steady-state velocity increases along a constant-$\eta$ line, the steady-state temperature remains constant. (Note that the curves in figures 3(*a*) and 4(*a*) are staggered.) It is clear from the figures that soon after the passage of the 'leading-edge' disturbance the steady-state values are approximated very well.

The second packet of oscillations on each of the curves has virtually identical frequency, phase and amplification characteristics to the 'leading-edge' disturbances. They are, however, up to a factor of 5 larger in amplitude. The temperature amplitude, for example, on figure 4(*a*) is as high as 2 °C (equivalent to $0.4\Delta T$). The cause, however, is not immediately apparent. Clearly, it is an isolated event – there are no other similar disturbances following it (at least not for the time span simulated). Furthermore, it appears to develop in a similar way to the first disturbance. That is to say, it originates near the base of the boundary and then amplifies in a narrow frequency band as it propagates up the boundary. This would imply that it does not represent a breakdown of the laminar boundary layer due to a transition to turbulence at some point where the Grashof number was sufficiently high. Instead it would appear that the boundary layer has again been perturbed in some way.

Following the passage of this second disturbance, the temperature and velocity traces start to diverge from the steady-state values. This is a direct result of the enclosed nature of the cavity starting to affect the flow. As a consequence the assumption of a semi-infinite plate no longer holds true. In the context of the cavity flow, however, two important results have emerged from detailed consideration of the vertical boundary layer. First, the two sets of oscillations in the boundary layer both produce frequencies that agree very closely with the high-frequency oscillations measured by Ivey (1984). Second, the amplitude of these oscillations, particularly those from the second disturbance also agree with the amplitudes measured by Ivey. The origin of only the first of these events can be accounted for by the flat-plate analysis, although the characteristics of the second are very similar. It will be necessary to consider the flow in the entire cavity to arrive at the cause of the second set.

### 5.2. *Cavity flow*

The cavity flow results produced as part of the present study confirm all the large-scale flow features reported in SPS. Where the results differ is that a number of small-scale features are now observable in the flow. Overall these do not appear to change the flow; however, there are pronounced local differences, particularly in the early stages of the flow. For a detailed description of the large-scale flow features the

reader is referred to SPS. The present cavity flow results will be used to consider three other aspects. These are the causes of the second set of short-period oscillations, the cavity-scale nature of the long-period oscillations, and the nature of the 'hydraulic jump' feature.

### 5.3. *Short-period oscillations*

A series of pathline plots (beginning with figure 5*a*) are used. The pathlines are the traces of 'particles' positioned at time $t = 0$ at every 8th mesh point. The points chosen on a particular row are displaced from those on the previous row by one mesh point (giving the impression of curved mesh lines). Although the computational timestep is 0.005 s, the 'particle' positions are upgraded only every 1 s by integrating the calculated velocity field at that instant. The dots on the figures are the particle positions at the beginning of the 10 s time span indicated. Temperature contours at the end of the time spans are also presented (beginning with figure 5*b*). The maximum and minimum contour values shown are 24.6 °C and 15.4 °C, and the interval between contours is 0.4 °C. Three of the four pairs of plots presented in figure 5 are at identical times to plots in figure 4 of SPS, allowing a comparison between the two solutions.

In figure 5(*a*), the pathlines show the high velocities up the hot (down the cold) boundary and the intrusions these produce across the top (bottom) of the cavity. The flow in the core of the cavity is dominated by entrainment into the vertical boundary layer and into the intrusions. The temperature contours in figure 5(*b*) support this description. They differ from the corresponding plot in SPS only in so much as the head of the intrusion appears to be defined in more detail here. Neither plot discerns the presence of the 'leading-edge' instability in the vertical boundary layers, as the perturbation amplitudes are too small.

Twenty seconds later, in figures 5(*c*) and 5(*d*), the top intrusion has just reached the opposite side of the cavity, and the 'piling up' of the intrusion fluid has commenced. This effect seems to be far more pronounced than the isotherm tilting due to entrainment into the cold wall boundary layer. However, the most important feature in figure 5(*d*) is the distortion to the vertical boundary layer caused by the 'impact' of the warm intrusion. The timing of this impact and of a similar one when the cool intrusion reaches the hot wall coincides exactly with the commencement of the second instability in the boundary layer. By considering the impact as a broad-band disturbance in a Fourier sense, it can be inferred that the same narrow-frequency band would be selectively amplified as with the leading-edge instability. Unlike that instability, however, the initial disturbance amplitude is relatively large, allowing for far greater amplitudes to be produced as the disturbance is convected along the boundary layer. Thus, it appears that the most immediate effect of the enclosed nature of the cavity on the boundary-layer flow is a far larger and more sudden one than would at first be expected. The disturbance in the vertical boundary layers is very noticeable a further twenty seconds on. Though it is not perceptible in the pathline plot of figure 5(*e*) (owing to the relatively small magnitude of the velocity component normal to the vertical boundary), it is very evident in the temperature contours of figure 5(*f*). Finally by time $t = 130$ s in figure 5(*h*) the disturbances in the boundary layers have been advected away and are now a part of the intrusions. This agrees with the results of figures 3 and 4.

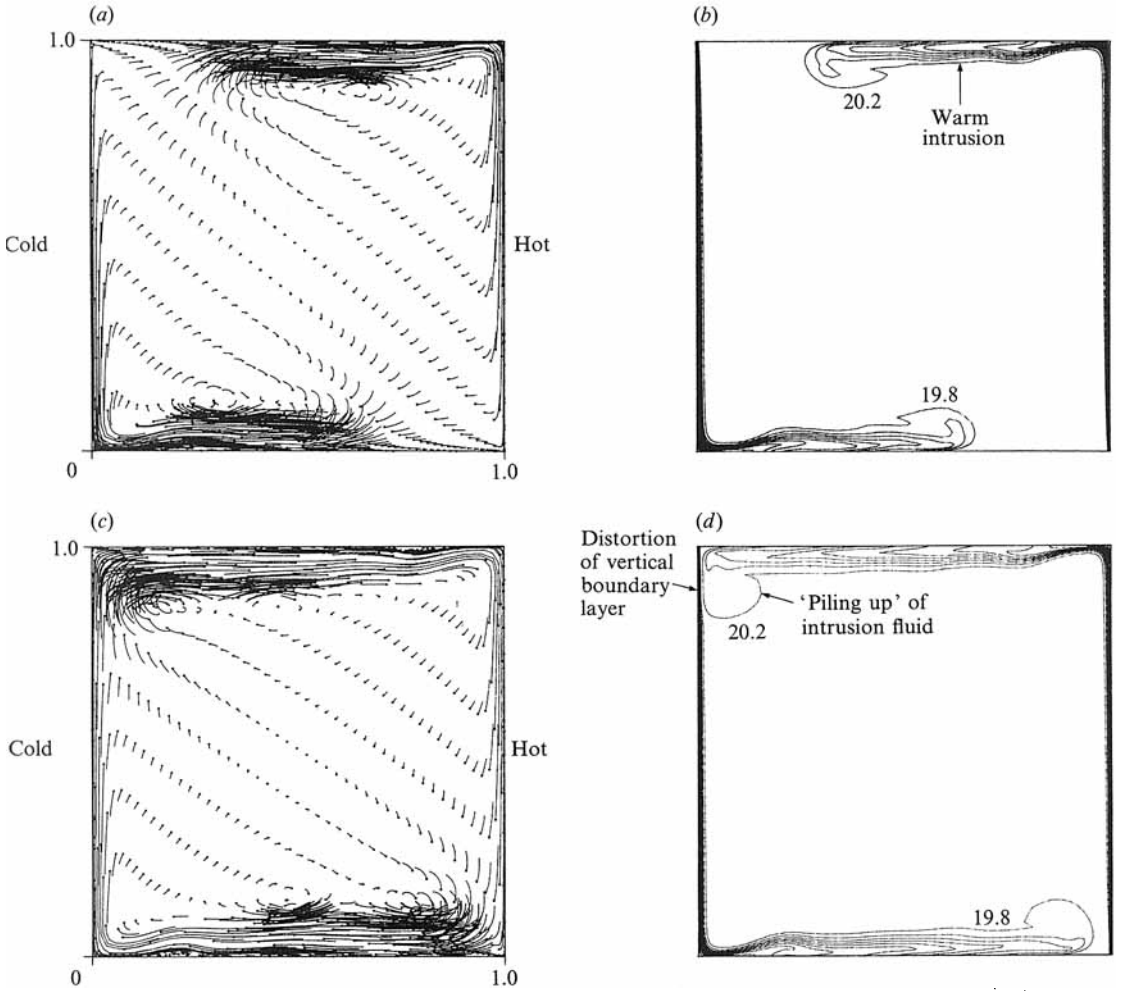


### 5.4. *Long-period oscillations*

The cavity-scale, long-period oscillations also commence with the arrival of the intrusions at the opposite side of the cavity and their subsequent 'piling up'. Within the head of the intrusions, flow reversals can be seen in figure 5(*e*) as the fluid commences to fall back. Compared to figure 5(*c*), velocities in the main body of the intrusions are noticeably smaller. The temperature contours in the intrusions (particularly the warm one) suggest the beginning of the collapse, as the isotherms commence tilting in the opposite direction in figure 5(*f*). In figure 5(*g*), the flow at the full extent of the collapse can be seen. Reversed flow exists along the full length of the intrusions. The temperature structure in figure 5(*h*) is showing an ever more complex temperature field, as the flow accommodates to the return flow in one direction and the continuing flux of boundary-layer fluid in the opposite. At later times, however, the growing complexity of the flow makes it difficult to know from just the inspection of the pathlines whether this is indeed a sustained, cavity-wide phenomenon.

A frequently used method for addressing such questions is to compute the energy

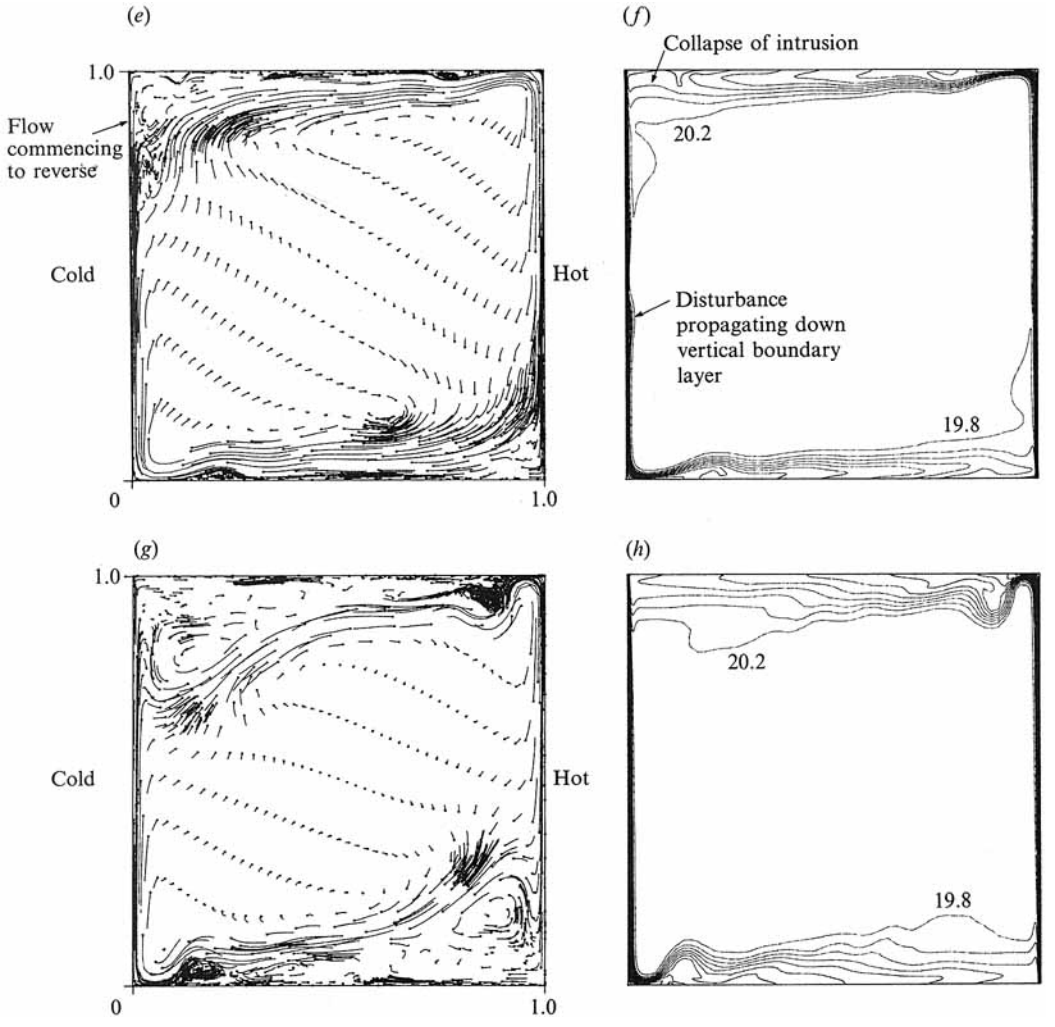


FIGURE 5. Evolution of the transient flow. Pathlines are for the time intervals (*a*) 40–50 s; (*c*) 60–70 s; (*e*) 80–90 s; (*g*) 120–130 s. Temperature contours are for (*b*) 50 s; (*d*) 70 s; (*f*) 90 s; (*h*) 130 s. Left wall is at 15 °C and right wall is at 25 °C. Dots on pathline plots are position of 'particle' at beginning of time span. Values shown on contour plots are in °C. Isotherms are at 0.4 °C intervals.

spectrum of a time series record of temperature or velocity at a point, and to identify the high-energy peaks. Such time series records were stored for the 17 points shown in figure 1. Inspection of the data showed that, for the period simulated, they were non-stationary in that at each point the record had a time-varying mean value, mean square value and frequency structure. As a result standard methods of time series analysis could not be used. An alternative approach to answering the question, while at the same time obtaining information about the evolution of the flow elsewhere in the cavity, is to use a simple type of interferogram.

Figure 6 is a set of profiles of the horizontal velocity component, $u$, midway across the cavity ($x/h = 0.5$). Each profile is 4 s apart, with the first at $t = 2$ s and the last at $t = 398$ s. Individual profiles have been staggered by 0.24 cm/s. The length of the box enclosing the figure corresponds to 2.5 cm/s, while the height corresponds to the

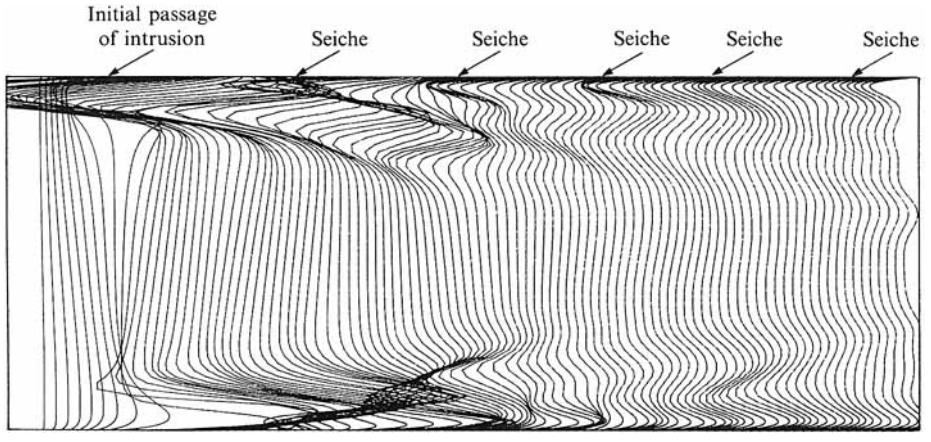


FIGURE 6. Profiles of the horizontal velocity component, $u$, at the vertical centreline of the cavity ($x/h = 0.5$). The profiles are at 4 s intervals, commencing with the profile at $t = 2$ s and ending with the profile at $t = 398$ s. Each profile is offset from the previous by 0.024 cm/s. The box length corresponds to 2.5 cm/s. The box height corresponds to the cavity height $h = 0.24$ m.

full cavity height, $h$. The purpose of this figure is not to elicit information about any individual profile (a difficult task in the early stages where profiles tend to overlay each other) but to provide a pattern of the entire flow history. Considering just the upper part of the figure (the warm intrusion) it can be recognized that the dark bands are due to the acceleration of the flow within the intrusion. The first (and largest) such event corresponds to the initial passage of the intrusion. Thereafter, it occurs on five occasions, each with progressively diminishing intensity. These commence at approximately 150, 210, 280, 330 and 390 s. These events represent successive cycles of the whole cavity wave. Flow reversals at the top of the intrusion only occur after the passage of the initial intrusion (as shown in figure 5$g$). Flow reversals immediately below the intrusion (to satisfy continuity) occur at every cycle.

Furthermore, as each cycle overflows its predecessors, a particular pattern of motion is gradually imposed on the entire cavity (including the core which at this stage is still isothermal). This pattern is one of alternating flow direction with height. Thus, the low-frequency, temporal periodicity of the intrusion, induces a secondary, spatial periodicity in the vertical structure.

The effect of the whole cavity mode is most apparent on the heat flux. This was shown by SPS by plotting the Nusselt number variation at the hot and cold walls and at the vertical centreline as a function of time. These are defined as

$$Nu_{\text{wall}} = \int_0^h \frac{K\dfrac{\partial T}{\partial x}}{\bar{K}(2\Delta T/l)}\,\mathrm{d}y, \tag{24}$$

and

$$Nu_{\text{cen}} = \int_0^h \frac{K\dfrac{\partial T}{\partial x} - C_p\rho Tu}{\bar{K}(2\Delta T/l)}\,\mathrm{d}y, \tag{25}$$

where $K$ is the thermal conductivity, $C_p$ is the specific heat at constant pressure, and the overbar indicates an average over the whole cavity. Figure 7 shows a similar plot derived from the present simulation results. The differences are immediately apparent. First, the effect of the two boundary-layer instabilities is superimposed on

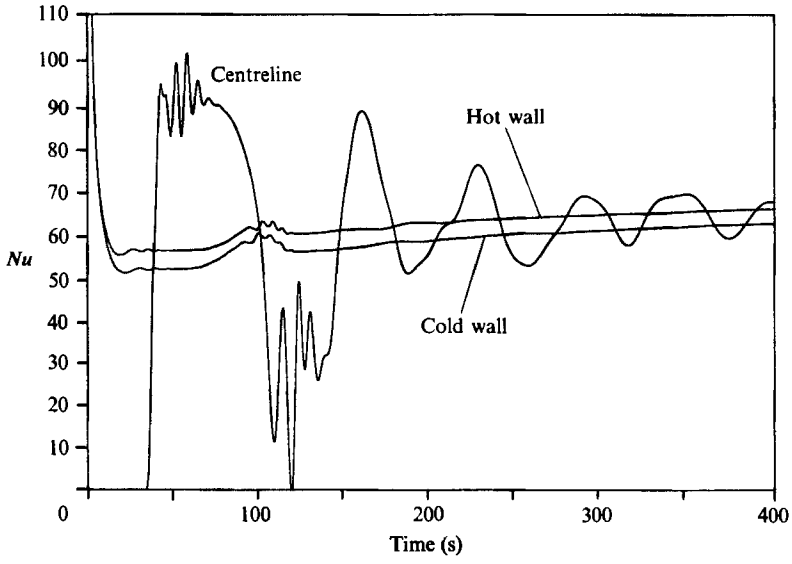


FIGURE 7. Nusselt number at the hot wall, cold wall and the vertical centreline as a function of time.

the low-frequency oscillation driven by the whole cavity mode at the centre of the cavity. The deviations in Nusselt number that these instabilities produce is of the order of the steady-state value. The effect, however, is relatively shortlived. This is not unexpected, as the frequency is greater than the Brunt–Väisälä frequency of the density-stratified intrusions, and so is rapidly damped. It also shows up in the wall Nusselt numbers, although to a much smaller degree. Second, the damping of the low-frequency oscillation is less than in the SPS result. This is not unexpected in the light of the lower numerical diffusivity of the present scheme. Overall, however, the large-scale heat transfer characteristics are very similar.

### 5.5. *Hydraulic jump*

Using the simulation results it is now possible to better describe the postulated 'hydraulic jump'. Indeed, it is not a hydraulic jump, but rather a complex recirculation zone that for a short period of time has a similar appearance. Again, the description is given with respect to the warm intrusion. In figures 5(*a*) and 5(*c*) this flow feature takes the form of a small separation zone. Possible reasons for the formation of the separation zone are presented in SPS. It is only in figure 5(*e*), when the intrusion is slowing down owing to the commencement of the return flow, that the zone gives some appearance of a hydraulic jump. This culminates in figure 5(*g*), where the zone has grown considerably in height and is the apparent centre of a very intense vortical flow.

Figures 8(*a*)–8(*d*) are enlargements of the top right-hand corner of the cavity. Figure 8(*a*) is for the time span $t = 120$–$125$ s. It shows that the flow feature in question is simply the result of the interaction of the return flow from the whole cavity wave (moving to the right) and the flow being discharged from the boundary layer (moving to the left). The return flow is forcing the main stream of the boundary discharge back towards the vertical boundary, and at the same time is being entrained into it. It is the entrainment that causes the appearance of the recirculation zone. As this happens, the boundary discharge is forced to flow ever more steeply. Between

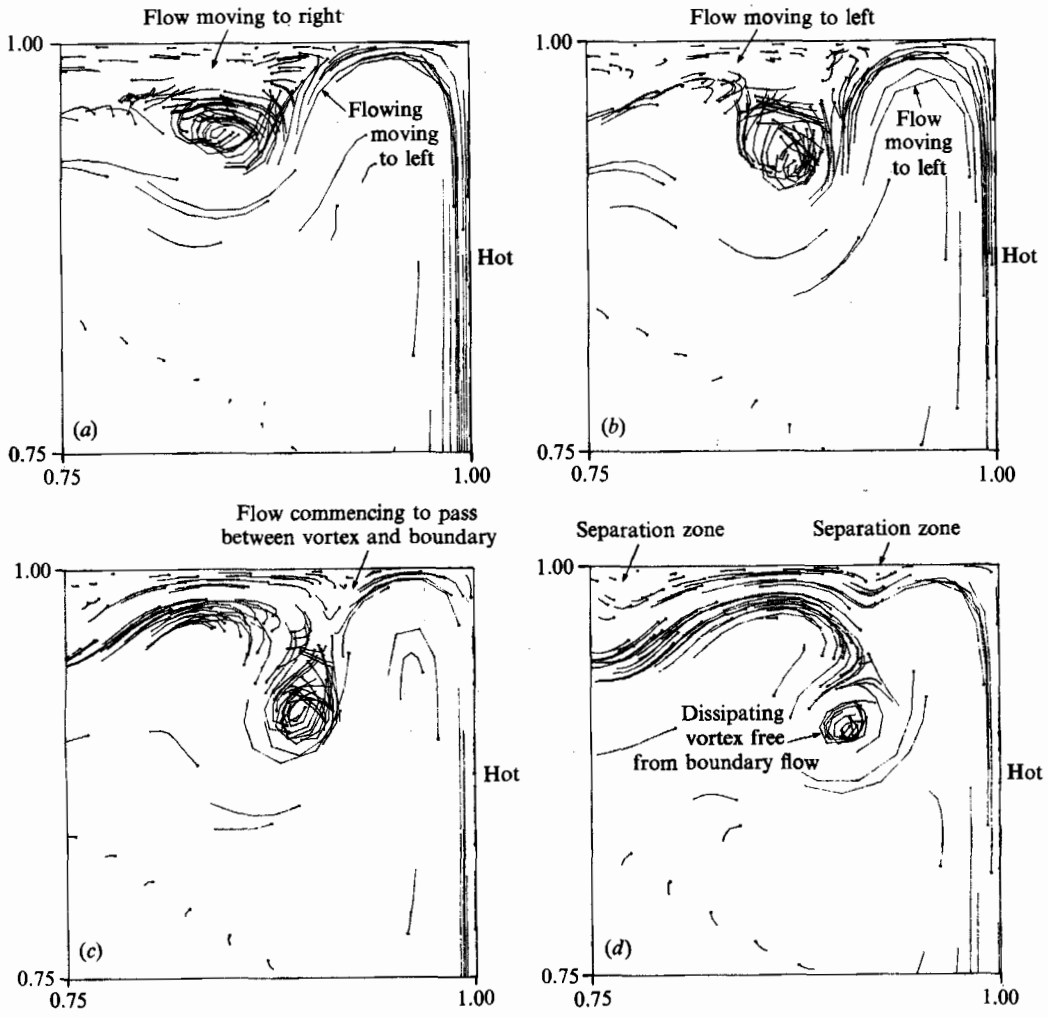


FIGURE 8. Pathlines in the upper right-hand corner of the cavity. The time intervals are (*a*) 120–125 s; (*b*) 125–130 s; (*c*) 130–135 s; (*d*) 135–140 s. Dots on pathline plots are position of 'particle' at beginning of time span.

$t = 125$–130 s in figure 5(*b*), the forcing back of the resulting recirculation zone is evident, as is the steepening of the discharge. The return flow has also reversed itself during this time span indicating that the whole cavity wave is now moving with the intrusion. The result of this is shown in figure 5(*c*), for the time span $t = 130$–135 s. The boundary discharge is now free to flow relatively unimpeded as it had previously. The simple separation zone is again established at approximately $x/h = 0.8$ on the cavity lid. A secondary separation zone is also present immediately adjacent to the recirculation at $x/h = 0.94$. The recirculation zone is now effectively cut off from the boundary flow and it proceeds to move away and decay, as evident 5 s later in figure 5(*d*). A similar series of events is repeated each time the whole cavity oscillation produces a flow in the opposite direction to the intrusion flow.

## 6. Conclusions

The results presented show that both long-period and short-period oscillations do exist during the early stages of transient flow in a side-heated cavity. The long-period, whole cavity oscillations are a result of the horizontal pressure gradients established by the tilting of the intrusion isotherms. The short-period oscillations arise owing to the amplification of two distinct instabilities in each of the thermal boundary layers. Each of the instabilities within a boundary layer has a different origin. The first is a result of the 'leading-edge' effect arising from the initial heating (cooling) of a boundary of finite length. Its evolution is well described by analogy to heating of a vertical plate. The second is a result of the disturbance to the boundary layer caused by the impact of the intruding flow from the opposite boundary. This instability grows in an identical way to the 'leading-edge' effect but attains a much larger amplitude. Both the amplitude and the frequency of the short-period oscillations are in good agreement with the measurements of Ivey (1984).

Both sets of short-period oscillations are advected into the intrusions, where they exert a marked influence on the heat flux across a vertical section of the cavity. This effect, however, is superimposed onto the larger contribution made by the whole cavity oscillation and is relatively short lived.

The whole cavity oscillations are a major component of the transient flow. Apart from the direct influence they exert on the intrusions within which they propagate, and the result this in turn has on the heat flux, they also determine the nature of the flow in the unstratified core of the cavity. By driving a system of essentially horizontal flows and counterflows, these oscillations impose a secondary, spatial wave form on the vertical structure.

Finally, the contention of a hydraulic jump contribution to the oscillations appears to be without foundation. What has been attributed to being a hydraulic jump in other numerical solutions and laboratory experiments is in fact shown to be no more than a complex recirculating zone arising from the interaction of the intrusions and the return flows.

This work was conducted with the support of the Division of Engineering and Geosciences, Office of Basic Energy Sciences, Department of Energy, USA through contracts No. DOE-DE-FG03-84ER13240 and DOE-DE-FG03-87-ER13757. The contribution of C. Y. Perng to the code development and the comments of my colleagues J. R. Koseff, R. L. Street and S. G. Monismith to an earlier draft are gratefully acknowledged.

## REFERENCES

Brown, S. N. & Riley, N. 1973 Flow past a suddenly heated vertical plate. *J. Fluid Mech.* **59**, 225–237.

Ede, A. J. 1967 Advances in free convection. *Adv. Heat Transfer* **4**, 1–64.

Gebhart, B. 1969 Natural convection flow, instability, and transition. *Trans. ASME* C: *J. Heat Transfer* **91**, 293–309.

Gebhart, B. 1973 Instability transition and turbulence in buoyancy induced flows. *Ann. Rev. Fluid Mech.* **5**, 213–246.

Gebhart, B. & Mahajan, R. L. 1982 Instability and transition in buoyancy-induced flows. *Adv. Appl. Mech.* **22**, 231–315.

Gill, A. E. 1966 The boundary layer regime for convection in a rectangular cavity. *J. Fluid Mech.* **26**, 515–536.

GILL, A. E. 1974 A theory of thermal oscillations in liquid metals. *J. Fluid Mech.* **64**, 577–588.

GOLDSTEIN, R. J. & BRIGGS, D. G. 1964 Transient free convection about vertical plates and circular cylinders. *Trans. ASME* C: *J. Heat Transfer* **86**, 490–500.

GRESHO, P. M., LEE, R. L., CHAN, S. T. & SANI, R. L. 1980 Solution of the time-dependent incompressible Navier–Stokes and Boussinesq equations using the Galerkin finite difference method. In *Approximation Methods for Navier–Stokes Problems*, Lecture Notes in Mathematics, vol. 771, pp. 203–222. Springer.

HIRT, C. W. 1968 Heuristic stability theory for finite-difference equations. *J. Comput. Phys.* **2**, 339–355.

HURLE, D. T. J., JAKEMAN, E. & JOHNSON, C. P. 1974 Convective temperature oscillations in molten gallium. *J. Fluid Mech.* **64**, 565–576.

INGHAM, D. B. 1978 Numerical results for flow past a suddenly heated vertical plate. *Phys. Fluids* **21**, 1891–1895.

INGHAM, D. B. 1985 Flow past a suddenly heated vertical plate. *Proc. R. Soc. Lond.* A **402**, 109–134.

IVEY, G. N. 1984 Experiments on transient natural convection in a cavity. *J. Fluid Mech.* **144**, 389–401.

JALURIA, Y. & GEBHART, B. 1973 An experimental study of non-linear disturbance behaviour in natural convection. *J. Fluid Mech.* **61**, 337–365.

JOSHI, Y. & GEBHART, B. 1987 Transition of transient vertical natural-convection flows in water. *J. Fluid Mech.* **179**, 407–438.

LEONARD, B. P. 1979 A stable and accurate convective modelling procedure based on quadratic upstream interpolation. *Computer Meth. Appl. Mech. Engng* **19**, 59–98.

MOLLENDORF, J. C. & GEBHART, B. 1970 An experimental study of vigorous transient natural convection. *Trans. ASME* C: *J. Heat Transfer* **92**, 628–634.

OSTRACH, S. 1952 An analysis of laminar free-convection flow and heat transfer about a flat plate parallel to the direction of the generating body force. *NACA TN* 2635, 47 pp.

PAOLUCCI, S. & CHENOWETH, D. R. 1989 Transition to chaos in a differentially heated vertical cavity. *J. Fluid Mech.* **201**, 379–410.

PATANKAR, S. V. 1980 *Numerical Heat Transfer and Fluid Flow.* Hemisphere. 197 pp.

PATTERSON, J. C. 1984 On the existence of an oscillatory approach to steady natural convection in cavities. *Trans. ASME* C: *J. Heat Transfer* **106**, 104–108.

PATTERSON, J. C. & IMBERGER, J. 1980 Unsteady natural convection in a rectangular cavity. *J. Fluid Mech.* **100**, 65–86.

PERNG, C. Y. & STREET, R. L. 1989 Three dimensional unsteady flow simulation: alternative strategies for volume averaged calculation. *Intl J. Numer. Meth. Fluids* (in press).

SCHLADOW, S. G., PATTERSON, J. C. & STREET, R. L. 1989 Transient flow in a side-heated cavity at high Rayleigh number: a numerical study. *J. Fluid Mech.* **200**, 121–148 (referred to as SPS).

SCHLADOW, S. G. & STREET, R. L. 1988 Transient flow in a weakly stratified side-heated cavity. *ASME FED* **71**, 39–41.

SIEGEL, R. 1958 Transient free convection from a vertical flat plate. *Trans. ASME* **80**, 347–359.

WORSTER, M. G. & LEITCH, A. M. 1985 Laminar free convection in confined regions. *J. Fluid Mech.* **156**, 301–319.